SiC Based On-Board EV Power-Hub with High-Efficiency DC Transfer Mode through AC Port for Vehicle-to-Vehicle Charging

Miad Nasr[1], Kshitij Gupta[2], Carlos da Silva[2], Cristina H. Amon[2], Olivier Trescases[1],
[1]Department of Electrical and Computer Engineering, University of Toronto,
[2]Department of Mechanical and Industrial Engineering, University of Toronto,
10 King's College Road, Toronto, ON, M5S 3G4, Canada
E-mail: miad.nasr@mail.utoronto.ca

***Abstract*— This paper is focused on a high-density, bi-directional, 6.6 kW EV power-hub, designed to operate in four distinct modes: 1) Grid-to-Vehicle (G2V), 2) Vehicle-to-Grid (V2G), 3) Vehicle-to-House (V2H), and 4) the more recent Vehicle-to-Vehicle (V2V) operating mode. This study also investigates sending DC power through a conventional 240 V_{RMS} Level-2 AC power port, with all the associated ratings and constraints from the AC design, in order to achieve higher power transfer and efficiency for V2V operation. Using a digital Hysteretic Current Mode Control (HCMC) scheme, the efficiency and loss distribution of four operating modes are analyzed: 1) dc-ac Boundary Conduction Mode (BCM), 2) dc-ac Continuous Conduction Mode (CCM)/BCM hybrid, 3) dc-dc BCM, and 4) dc-dc CCM. The AC design achieves a peak efficiency of 96.6% and an average THD of 3.2%. The peak efficiency of the power-hub is increased from 96.6% to 98.3%, by operating in DC transfer mode for V2V operation, thus increasing the power capability by 50%. Finally, a new low-frequency output voltage commutation scheme is proposed to reduce the peak junction temperature of MOSFETs when operating in V2V dc-dc mode.**

I. Introduction

Although the automotive industry has experienced a sevenfold increase in the global sales of Plug-in Electric Vehicles (PEVs) since 2011 [1], range anxiety and slow charging times still remain the most significant obstacle to the widespread adoption of PEVs. The biggest fear of any EV owner is the possibility of being stranded in the middle of the interstate highway with a completely discharged battery. Alternatively, the EV may become totally discharged if left unattended and unplugged at low State-of-Charge (SOC) in a parking lot. With today's state of EV support infrastructure, the current solution is to tow the vehicle to the nearest charging station. Previous work on bi-directional EV battery chargers have focused on the Vehicle-to-Grid (V2G) [2]–[4], and Vehicle-to-House (V2H) modes of operation [5]–[8]. V2G mode allows the power-hub to transfer energy from the High-Voltage (HV) battery to the grid during peak hours of the day or night and, as a result, reduce the electricity cost to the user. In the case that the user drives to an off-grid cottage, V2H mode is used to power AC appliances from the EV. V2H mode can also be used in construction or emergency response applications. In this study, a high power-density, four-quadrant EV power-hub is developed and a novel Vehicle-to-Vehicle (V2V) charge transfer mechanism is investigated, which allows two EVs to share charge in case one has a depleted battery. The proposed design is an all-in-one power-hub capable of operating in V2G, G2V, V2H, and V2V operating modes, as shown in Fig. 1(a).

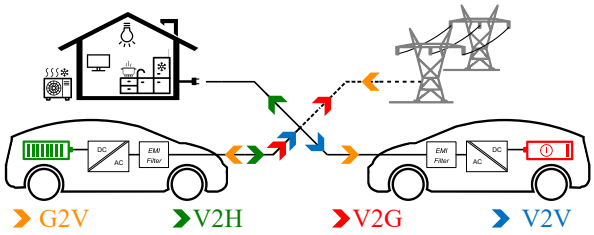

(a)

(b)

Fig. 1. (a) Different operating modes of a bi-directional EV power-hub, namely G2V, V2G, V2H, and V2V. (b) Custom pickup truck EV targeted in this paper.

This power-hub is intended for use in a full-electric pick-up truck prototype, as shown in Fig. 1(b), with a fully custom 450V Li-ion battery pack. The main goal of this study is to investigate sending DC power through a conventional 240 V_{RMS} Level-2 AC power port, while operating in V2V mode, with all the associated ratings and constraints from the AC design, in order to achieve higher power transfer and efficiency. The Hysteretic Current Mode Control (HCMC) architecture is described in Section II, the design procedure for the EMI filter is outlined in Section III, and the basics of V2V, and the dc-dc operating mode is introduced in Section IV. Finally, the experimental results of the power-hub operating in the dc-ac and dc-dc modes are presented in Section V, along with a detailed loss analysis.

978-1-5386-1180-7/18/$31.00 ©2018 IEEE

II. Inverter Architecture and Control

The power-hub is implemented as a two-stage bi-directional converter, with a Dual-Active-Bridge (DAB) converter regulating the battery current and a Full-Bridge dc-ac converter performing Power Factor Correction (PFC) and regulating the DC link bus voltage, V_{in}. This study focuses on the dc-ac power-stage performance. Unlike conventional sinusoidal Pulse-Width-Modulation (PWM) [9], the dc-ac power-stage operates in Hysteretic Current Mode Control (HCMC). The peak and valley of the inductor current, $i_L(t)$, are digitally controlled on a cycle-by-cycle basis using a set of 12-bit Digital-to-Analog Converters (DACs), a high-bandwidth current sense amplifier and two comparators. By switching the MOSFETs in a complementary fashion, a single low-side shunt resistor, R_{sense}, is used for sensing both the rising and falling inductor current, as shown in Fig. 2.

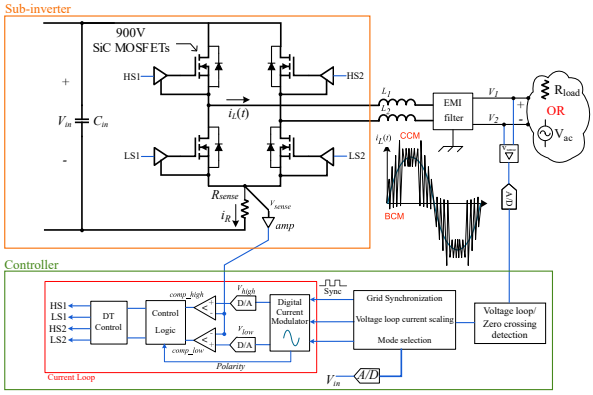

Fig. 2. Architecture of the full-bridge inverter topology and hysteretic current-mode controller.

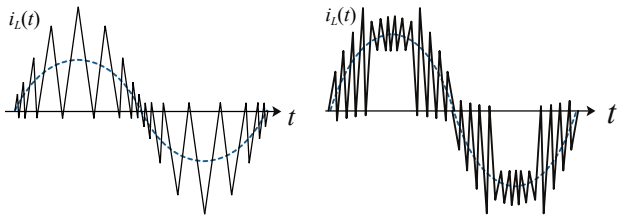

(a) (b)

Fig. 3. The power-hub is designed for AC power transfer in the (a) BCM, or (b) BCM/CCM hybrid operating mode. The controller switches to hybrid mode from BCM at higher power-levels.

Using this scheme, the sensed voltage, V_{sense}, across R_{sense} rapidly changes polarity as one set of switches commutates, as shown in Fig. 4(a). A digital controller is used for precise current control and a 60 Hz synchronization pulse, *sync*, is used for grid phase locking in G2V (charging) and V2G operating modes. The digital current reference is scaled by the controller as part of the outer voltage loop. The inverter operates in two possible modes throughout the AC line-cycle: 1) Boundary Conduction Mode (BCM) or 2) Continuous Conduction Mode (CCM). When operating in BCM, a slightly negative valley current, I_{valley}, is imposed to achieve zero-voltage turn-on of the MOSFETs through the resonance of the switching node capacitance and main inductor. BCM results in the lowest switching losses, at the expense of higher RMS conduction and core losses in the inductors.

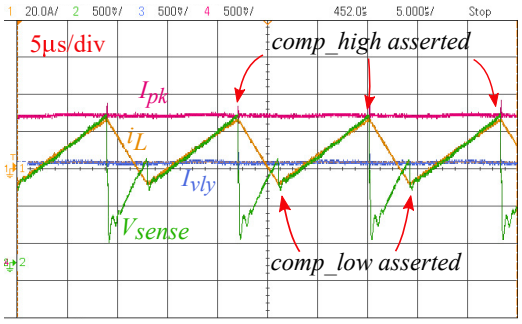

(a)

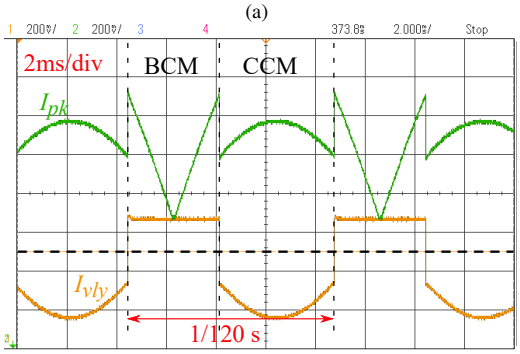

(b)

Fig. 4. HCMC operation with the (a) i_L and I_R waveforms and instances when the comparator output signals are asserted in BCM operation. (b) Peak and valley envelopes for the inductor current for a line cycle in hybrid mode operation.

In [10], a three-mode DCM/BCM/CCM current mode controller is implemented on a 150 W, 1 MHz, PFC boost rectifier with GaN technology. A BCM dual-mode ZVS/ZCS current control scheme is introduced in [11], in which the controller sets the valley current limit below zero near the zero crossings and at zero near the peaks and troughs of the AC line-cycle.

In this work, the inverter automatically switches into CCM to minimize core losses and limit the saturation current requirement of the inductors at the highest current-level. This operating mode is denoted as hybrid mode throughout this paper. The ideal inductor current waveforms for the BCM and hybrid operation is shown in Figs. 3(a) and (b), respectively, and the line frequency peak and valley current limit modulation is shown in Fig. 4(b). The major advantage of the hybrid scheme is that the power density of the converter can be significantly increased, since inductors with a lower saturation current can be used. The inverter has a variable switching frequency based on HCMC operation, which helps to reduce the EMI filter size due to the spread-spectrum effect. While the SiC-based inverter can easily operate above 500 kHz, the frequency is limited to 250 kHz for optimal efficiency.

III. EMI Filter Design

International standards such as CISPR 16 [12] and IEC61000 [13] provide limits on the magnitude of output current harmonics in the range of 150 kHz to 30 MHz, for residential and industrial equipment. The increase in switching frequency above 150 kHz makes the design of the EMI filter especially challenging due to the extra attenuation needed for meeting EMC requirements. EMI filters for dc-ac inverters are typically composed of a differential filter, for filtering differential noise, and a common-mode filter, for suppressing common-mode noise. For the purposes of this study, only conducted EMI emission compliance was taken into account.

To begin the design of an EMI filter, the spectral content of the inductor current waveform without an EMI filter must be known. Detailed mixed-mode Cadence simulations were performed with an exact implementation of the digital controller to obtain the power inductor current without an EMI filter. A CISPR16 [12] Line Impedance Stabilization Network (LISN) was included in the simulation to obtain the noise spectrum of the grid current, i_g, at the full power-level of 6.6 kW. The simulated noise spectrum of the LISN output in this case along with the CISPR16 class A and B limits are plotted in Fig. 6(a).

According to [14], the required filter attenuation at the peak harmonic frequency is given by:

$$U_{req} = U_{peak} - U_{limit} + SM, \tag{1}$$

where U_{peak} is the peak harmonic magnitude in dBμV at the peak harmonic frequency, f_{peak}, U_{limit} is the CISPR16 limit in dBμV at f_{peak}, and SM is a safety margin set to 12 dBμV. According to Fig. 6(a), within the frequency range of the CISPR16 limits, U_{peak} = 143 dBμV occuring at f_{peak} = 152.3 kHz. This results in a required attenuation, U_{req}, of 98 dBμV. Assuming a two stage LC filter design with both poles placed before f_{peak}, we have:

$$L_{DM}C_{DM} = \frac{10^{\frac{U_{req}}{30}}}{4\pi^2 f_{peak}^2}, \tag{2}$$

where L_{DM} and C_{DM} are the differential-mode filter component values as derived in [15]. It is claimed in [16] that to ensure a high displacement power factor, C_{DM} must be limited according to the following:

$$C_{DM} < \frac{P_{out} tan(cos^{-1}(PF_{dp}))}{\eta V_{in}^2 2\pi f_{line}}, \tag{3}$$

where PF_{dp} is the minimum displacement power factor required. To achieve a minimum PF_{dp} of 0.999 at the maximum power-level of 6.6 kW and a V_{in} of 240 V_{RMS} at 60 Hz, a C_{DM} less than 14 μF is required. Using the results obtained from (2), an $L_{DM} > 280.9$ μH is necessary. To design the common-mode stage of the EMI filter, the second LC pole is place half way between the first LC pole and f_{peak}. In order to effectively filter common-mode noise, common-mode chokes and Y capacitors between the phase and neutral lines to earth are utilized. The equivalent Y capacitance at the second LC stage is limited to:

$$C_{Y\_eq} = \frac{I_{leakage}}{V_{in} 2\pi f_{line}}. \tag{4}$$

where $I_{leakage}$ is the earth leakage current and is set to 3.5 mA according to the CISPR 22 standard specifications [17]. This results in C_{Y_eq} = 38.7 nF and L_{CM} = 1.4 mH. Using the component values calculated, the final designed EMI filter and it's input to output current transfer function are shown in Figs. 5(a) and (b), respectively.

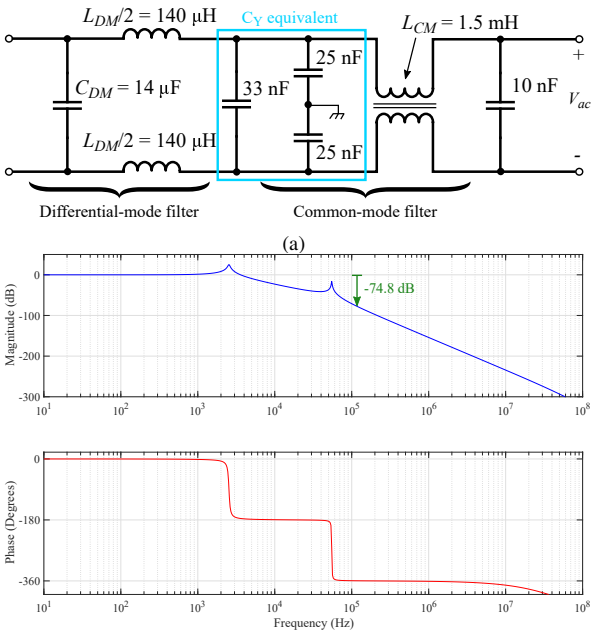

Fig. 5. (a) EMI filter designed for the power-hub. (b) Input-to-output current transfer function of the EMI filter.

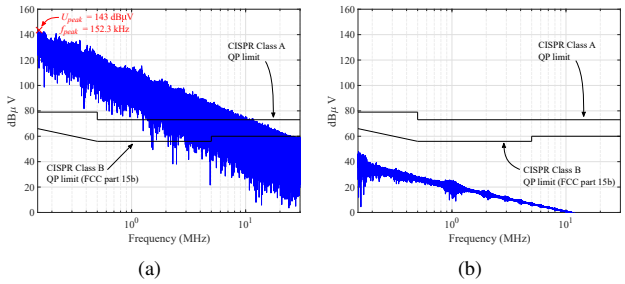

Fig. 6. Simulated frequency spectrum of the LISN output with the inverter operating (a) without and (b) with the designed EMI filter at 6.6 kW.

To test the performance of the designed EMI filter, another set of Cadence simulation was run with the EMI filter in the circuit. As a conducted EMI pre-compliance measure, the CISPR22 spectrum limits are overlayed on Fig. 6(b) and clearly shows that the designed EMI filter is attenuating the current harmonics by 78 dB, in comparison to the original spectrum shown in Fig. 6(a).

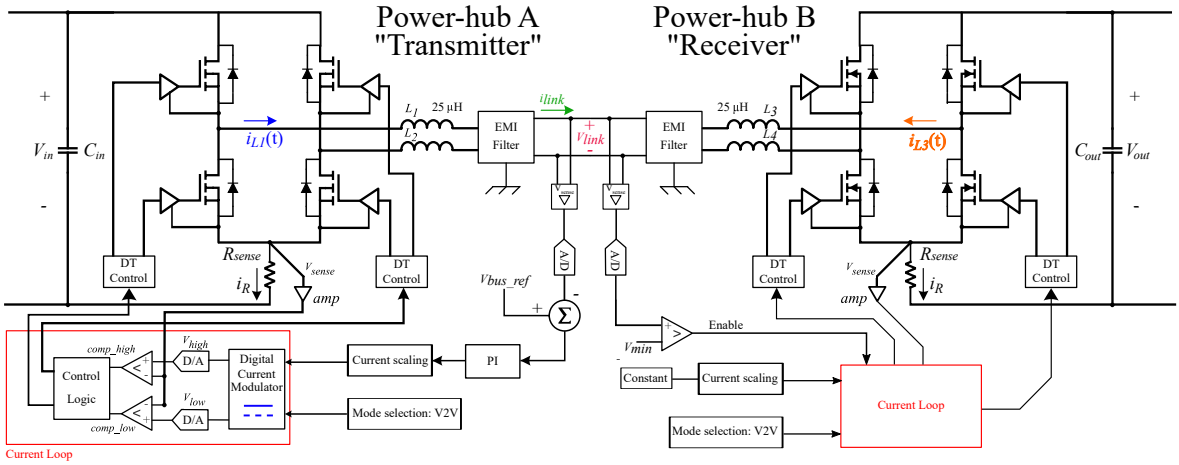

Fig. 7. Two power-hubs, which are designed and optimized for AC power transfer, are setup in V2V mode to transfer DC power.

IV. V2V Operating Mode

Two power-hubs connected together can either interchange DC or AC power. The AC power transfer solution faces many challenges, since it is not possible to maintain a low THD sine wave under no-load conditions because of the HCMC controller requirements. Since the receiving EV needs to synchronize to an AC voltage at first, a no-load condition is inevitable at startup. By transferring DC power, the converter continuously operates at the peak voltage of the AC line cycle (340 V for 240 V_{RMS} AC systems) with a lower current to achieve the same output power, resulting in lower conduction losses, lower switching frequency, and a higher efficiency. DC power transfer also allows the converter to operate beyond it's intended AC power rating, which results in a shorter charging time and a faster revival of the depleted battery.

During DC power transfer, the power-hub can either operate in BCM or CCM, depending on the target power-level. This is similar to AC power transfer, where the power-hub is operable in BCM or hybrid BCM/CCM. At lower power-levels, the controller imposes a slight negative valley current to ensure soft turn-on of the MOSFETs. To reach higher power-levels, the valley current is increased by the HCMC controller, resulting in the loss of soft-switching, higher switching frequency, but lower RMS current in the inductors.

In V2V mode, the output ports of power-hub A (Transmitter) and B (Receiver) are connected as shown in Fig. 7, and the link voltage, V_{link}, is regulated by power-hub A to a set reference, V_{bus_ref}, as part of an outer voltage loop. Each EMI filter, which is optimized for the AC charging operation, includes 10μF of capacitance that is necessary for the HCMC controller operation and eliminates the need for an external DC link capacitor. Once V_{link} rises above a predetermined threshold, V_{min}, power-hub B is enabled and begins charging the depleted HV battery. The auxiliary supply voltages for each power-hub are derived from a secondary Low-Voltage (LV) battery and a self-regulating universal dc-ac adapter connected to the output port of the converter. These two independent voltage sources are diode-ORed to prevent any black-out condition especially for power-hub B, which might also have a depleted LV auxiliary battery.

V. Implementation and Experimental Results

The power-hub, as shown in Fig. 8, is realized with paralleled 900V, 35 A, 65 mΩ R_{on} SiC MOSFETs [18]. The two high-side MOSFET pairs are placed on the top side of the PCB, and the two low-side MOSFET pairs are placed underneath the high-side MOSFETs on the bottom side of the PCB. Utilizing both sides of the PCB for MOSFET placement, improves the electrical performance of the inverter by reducing the loop parasitic inductance. However, the thermal design becomes more challenging. The four high-side MOSFETs and the four low-side MOSFETs have a dedicated 6A isolated gate driver with a 12 V drive voltage. The two 25 μH, 45 A line inductors are custom-made with AWG-9 litz wire and an ETD44 ferrite core. The thermal system design includes a custom liquid cooling chill plate for the MOSFETs (not included in the preliminary prototype) and air cooling for the power inductors. Liquid cooling cannot effectively be used for the inductors, since high switching frequency operation of the converter creates eddy current losses within conductive heat-sinks.

TABLE I
Power-hub Inverter Specifications

Parameter	Value	Unit
Input voltage, V_{in}	450	V_{DC}
Output voltage, V_{out}	240	V_{RMS}
Input capacitance, C_{in}	970	μF
Line inductance, $L_1 + L_2$	50	μH
Peak AC power	6.6	kW
Peak AC efficiency (4.3 kW)	96.6	%
Max switching frequency	200	kHz
Min switching frequency	30	kHz
MOSFETs	C3M0065090J, Wolfspeed SiC D^2PAK, 900 V, 35 A, 65 mΩ	

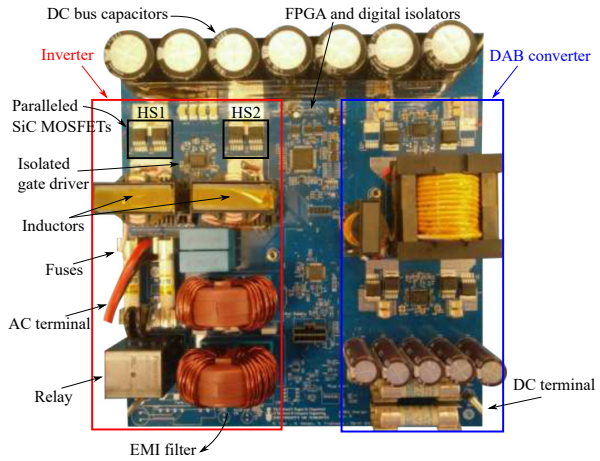

Fig. 8. Top side view of the EV power-hub PCB containing the inverter and a DAB dc-dc converter. The DAB converter is outside the scope of this paper.

The measured operation of the power-hub in the dc-ac BCM mode at 2.3 kW, dc-ac hybrid mode at 5 kW, dc-dc BCM mode at 3.4 kW, and dc-dc CCM at 5.3 kW are shown in Figs. 9(a), (b), (c), and (d), respectively. The operation of two power-hubs in V2V configuration at a power-level of 1 kW is shown in Fig. 11.

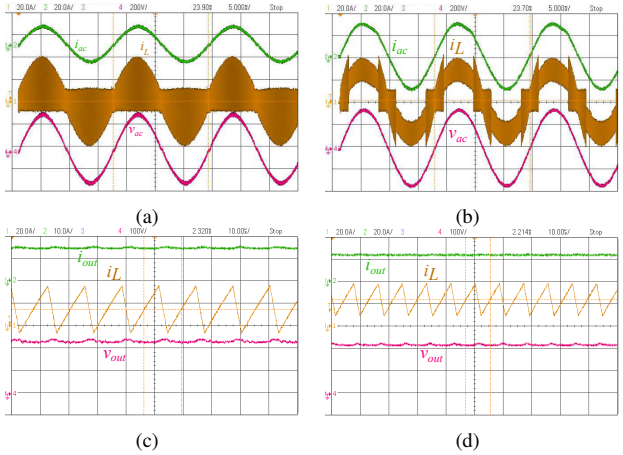

Fig. 9. Operation of the EV charger in the (a) dc-ac BCM at 2.3 kW, (b) dc-ac BCM/CCM hybrid at 5 kW (c) dc-dc BCM at 3.4 kW, and (d) dc-dc CCM operating mode at 5.3 kW. All waveforms are taken with 450 VDC input and an output of 240 V_{RMS} and 240 VDC in the dc-ac and dc-dc cases, respectively.

The measured efficiency of the power-hub versus output power in the dc-ac and dc-dc operating modes is shown in Fig. 10. As opposed to the dc-ac mode, a constant DC output voltage in the dc-dc operating mode results in higher achievable power-levels. For the same average inductor current, the power-level increases proportional to the output DC voltage. In the BCM only mode, there is an increase in efficiency going from dc-ac to dc-dc operation and with higher output DC voltages, due to lower switching frequencies and lower conduction losses. It must be noted that this power-hub is optimized for AC power transfer and therefore, the output over-voltage protection circuitry limits V_{link} to 340 V_{peak}. Due to a higher achievable efficiency than in dc-ac mode, the converter can operate at 1.5× it's rated AC power capability for the same thermal design, even though CCM mode introduces hard-switching and an increased switching frequency.

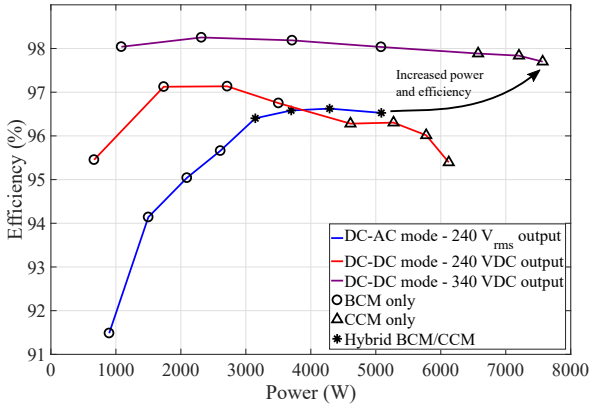

Fig. 10. Measured efficiency of the power-hub inverter operating in dc-ac at 240 Vrms and dc-dc mode at 240 VDC and 340 VDC.

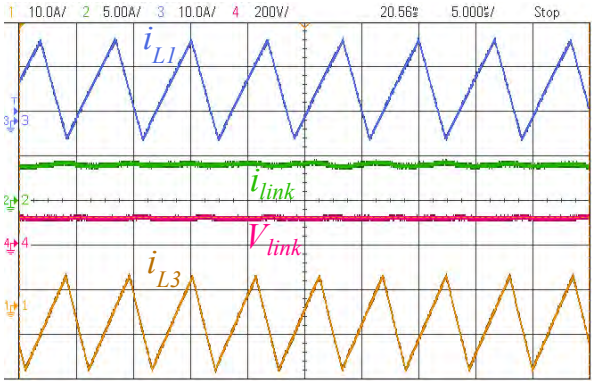

Fig. 11. Measured waveforms demonstrating the operation of the two power-hubs in V2V mode.

A. Loss Analysis

Detailed mixed-mode Cadence simulations were performed with the C3M0065090J MOSFET spice model and an exact implementation of the digital controller to characterize the loss distribution of the power-hub in each of the four modes of operation. The simulation includes HDL models for the controller and Verilog-a models for data converters. In the dc-ac BCM case, inductor core loss is the most significant source of loss and MOSFET switching losses comprise only 22% of the total power dissipation, as evident in Fig. 12(a). This is because of the large inductor current ripple and ZVS turn-on of the MOSFETs. In the dc-ac hybrid mode, switching losses are significantly increased due to the loss of soft-switching at the line cycle peaks and troughs, as shown in Fig. 12(b). The inductor core losses are, however, decreased due to lower current ripple. The dc-dc BCM operating mode

is least dissipative due to soft-switching and having the lowest switching frequency. In the dc-dc CCM case, the losses are still lower than the dc-ac hybrid mode, even though the power-level is 2 kW higher, as presented in Figs. 12(d) and (b).

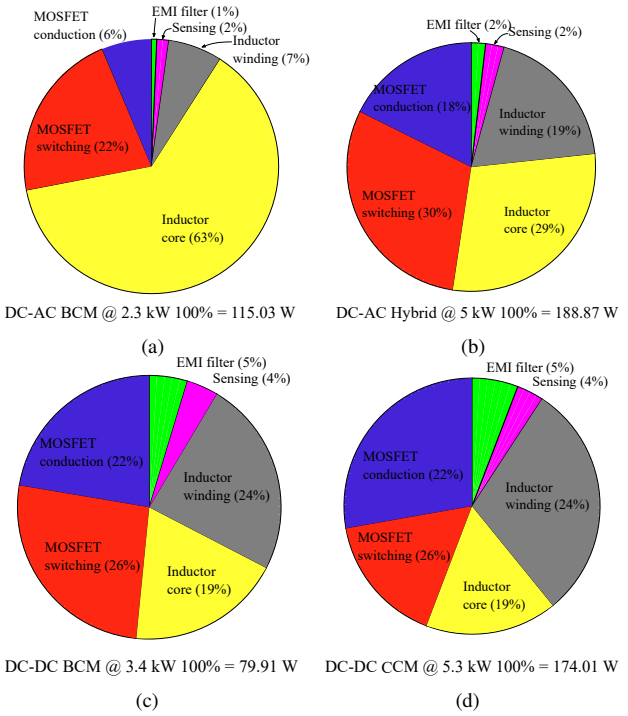

Fig. 12. Simulated loss breakdown of the power-hub in the (a) dc-ac BCM (2.3 kW), (b) dc-ac BCM/CCM hybrid (5 kW), (c) dc-dc BCM (3.4 kW), and (d) dc-dc CCM operating mode (5.3 kW). Vin=450 VDC, Vout=340 VDC.

B. Bipolar V_{Link} Regulation

Due to the high duty-cycle operation in the dc-dc mode, which is caused by the high output DC voltage, there is an uneven distribution of losses among the MOSFETs. A promising solution, as shown in Fig. 13(b), is to commutate the polarity of V_{link} at a very low frequency. This prevents each MOSFET from reaching steady-state thermal equilibrium, leading to a lower peak junction temperature. Similar techniques have been demonstrated for fault-tolerant LED lighting applications [19]. A thermal model is built in PLECS with the extracted switching loss model from Cadence and estimation of the thermal resistance and capacitances to simulate the proposed bipolar V_{link} scheme. The effect of this scheme on the junction temperature of the MOSFETs is shown in Fig. 13(b). This can be compared to the case without commutation, as shown in Fig. 13(a).

The optimal commutation frequency, $f_c = 1/T_c$, is heavily dependent on the implemented thermal system, and more specifically, on the thermal capacitance and thermal resistance of the MOSFETs to ambient. The thermal system implemented in this work yielded an optimal commutation frequency of 5 Hz to prevent the MOSFETs from reaching thermal steady-state.

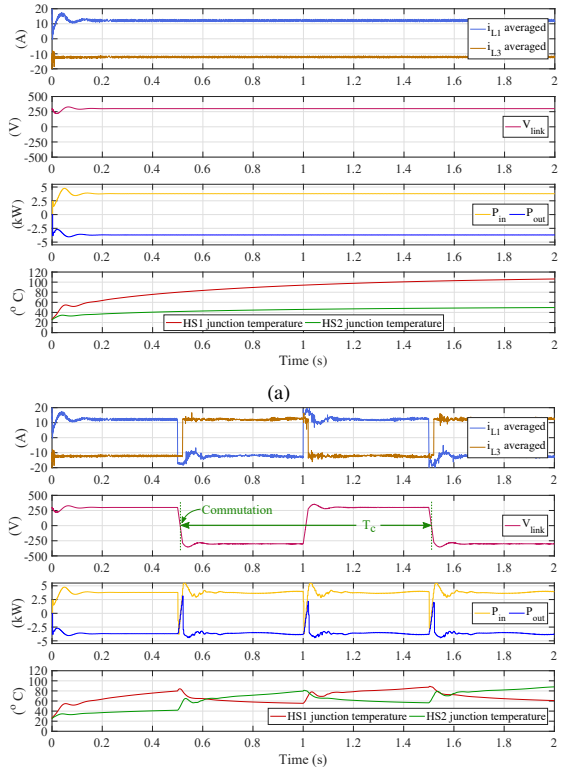

Fig. 13. (a) Simulated operation of two power-hubs in V2V mode with (a) constant DC and (b) bipolar V_{link} regulation. Commutating V_{link} at 1 Hz results in 16°C lower average and 17°C lower peak MOSFET junction temperature.

The bipolar operation of the power-hub at a 2 kW power-level with $f_c = 5$ Hz is shown in Fig. 14. The measured thermal performance of the power-hub in the dc-dc mode with unipolar and bipolar V_{link} regulation is shown in Figs. 15(a) and (b), respectively. The MOSFETs are air-cooled with aluminum heat sinks and the converter is operated for 5 minutes at 2 kW. The input voltage is 420 VDC and the output voltage is regulated to ±340 VDC in bipolar operation. With bipolar operation, the peak MOSFET case temperature is reduced by 6°C, while the junction temperature is reduced by an estimated 10.3°C.

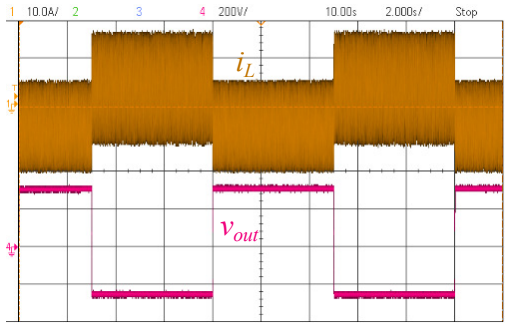

Fig. 14. Measured bipolar V_{link} regulation of the EV power-hub with f_c = 5 Hz. To prevent unwanted EMI issues caused by the V_{link} polarity transition points, the peak current limit is gradually reduced to less than 7 A, in a duration of 5 ms, before reversing the polarity of V_{link}.

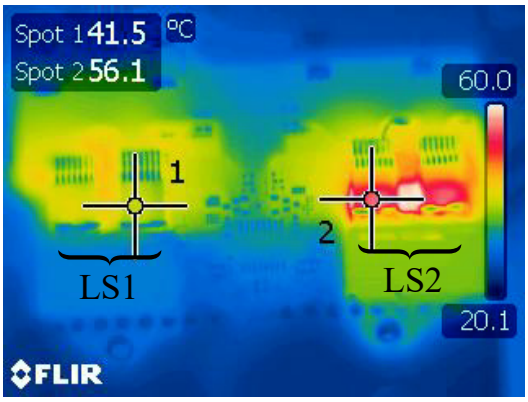

(a)

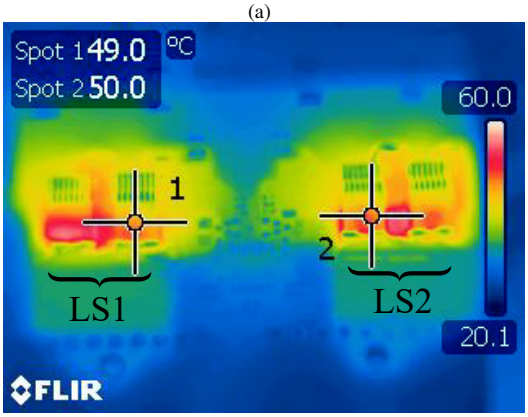

(b)

Fig. 15. Thermal performance of the power-hub operating in dc-dc mode showing the temperature of the two low-side MOSFET pairs with (a) constant DC V_{link} regulation, and (b) bipolar V_{link} regulation. The optimal V_{link} commutation frequency of 5 Hz results in 6°C lower peak MOSFET temperature.

VI. Conclusions

A bi-directional EV power-hub has been designed and implemented using a dual-mode BCM/hybrid HCMC controller, to achieve an excellent trade-off between efficiency and power density. The hybrid control scheme combines the soft-switching benefits of BCM with the lower inductor current ripple advantages of CCM. This allows the utilization of inductors with lower saturation current, and hence, lower system volume. The power-hub is also verified to operate in V2V mode by transferring DC power through the AC port of the converter. This results in a 50% increase in power-level and a 7.8% decrease in losses without compromising thermal performance and reliability. A bipolar V_{link} regulation scheme is also proposed to equalize the loss distribution among the power-stage MOSFETs. With a 5 Hz commutation frequency, 10.6% lower MOSFET case temperature is observed at a power-level of 2 kW.

Acknowledgements

The authors thank Tony Han and Havelaar Canada for their support of the UofT Electric Vehicle Research Centre. This work was also supported by The Natural Sciences and Engineering Research Council of Canada (NSERC). Mazhar Moshirvaziri provided valuable technical guidance in this project.

References

[1] "Global trends in renewable energy investment 2016," Frankfurt School of Finance and Management, Tech. Rep., 2016. [Online]. Available: http://fs-unep-centre.org/sites/default/files/publications/

[2] H. Wang, X. Jia, J. Li, X. Guo, B. Wang, and X. Wang, "New single-stage ev charger for v2h applications," in *2016 IEEE 8th International Power Electronics and Motion Control Conference (IPEMC-ECCE Asia)*, May 2016, pp. 2699–2702.

[3] J. G. Pinto, V. Monteiro, H. Gonalves, B. Exposto, D. Pedrosa, C. Couto, and J. L. Afonso, "Bidirectional battery charger with grid-to-vehicle, vehicle-to-grid and vehicle-to-home technologies," in *IECON 2013 - 39th Annual Conference of the IEEE Industrial Electronics Society*, Nov 2013, pp. 5934–5939.

[4] M. Kwon, S. Jung, and S. Choi, "A high efficiency bi-directional ev charger with seamless mode transfer for v2g and v2h application," in *2015 IEEE Energy Conversion Congress and Exposition (ECCE)*, Sept 2015, pp. 5394–5399.

[5] C. Jiang, B. Lei, H. Teng, and H. K. Bai, "The power-loss analysis and efficiency maximization of a silicon-carbide mosfet based three-phase 10kw bi-directional ev charger using variable-dc-bus control," in *2016 IEEE Energy Conversion Congress and Exposition (ECCE)*, Sept 2016, pp. 1–6.

[6] C. Liu, J. Wang, K. Colombage, C. Gould, and B. Sen, "A cllc resonant converter based bidirectional ev charger with maximum efficiency tracking," in *8th IET International Conference on Power Electronics, Machines and Drives (PEMD 2016)*, April 2016, pp. 1–6.

[7] B. Kramer, S. Chakraborty, and B. Kroposki, "A review of plug-in vehicles and vehicle-to-grid capability," in *2008 34th Annual Conference of IEEE Industrial Electronics*, Nov 2008, pp. 2278–2283.

[8] R. Zgheib, K. Al-Haddad, and I. Kamwa, "V2g, g2v and active filter operation of a bidirectional battery charger for electric vehicles," in *2016 IEEE International Conference on Industrial Technology (ICIT)*, March 2016, pp. 1260–1265.

[9] S. R. Bowes, "New sinusoidal pulsewidth-modulated invertor," *Electrical Engineers, Proceedings of the Institution of*, vol. 122, no. 11, pp. 1279–1285, November 1975.

[10] R. Fernandes and O. Trescases, "A multimode 1-mhz pfc front end with digital peak current modulation," *IEEE Transactions on Power Electronics*, vol. 31, no. 8, pp. 5694–5708, Aug 2016.

[11] A. Amirahmadi, L. Chen, U. Somani, H. Hu, N. Kutkut, and I. Bartarseh, "High efficiency dual-mode current modulation method for low-power dc/ac inverters," *IEEE Transactions on Power Electronics*, vol. 29, no. 6, pp. 2638–2642, June 2014.

[12] "Specification for radio disturbance and immunity measuring apparatus and methods - Part 1-2: Radio disturbance and immunity measuring apparatus - Coupling devices for conducted disturbance measurements," Canadian Standards Association, Ontario, Canada, Standard, Mar. 2014.

[13] "Electromagnetic compatibility (EMC) - Part 3-2: Limits - Limits for harmonic current emissions (equipment input current; 16 A per phase)," International Electrotechnical Commission, Geneva, CH, Standard, May 2014.

[14] K. Raggl, T. Nussbaumer, and J. W. Kolar, "Guideline for a simplified differential-mode emi filter design," *IEEE Transactions on Industrial Electronics*, vol. 57, no. 3, pp. 1031–1040, March 2010.

[15] G. Ala, G. C. Giaconia, G. Giglia, M. C. D. Piazza, M. Luna, G. Vitale, and P. Zanchetta, "Optimized design of high power density emi filters for power electronic converters," in *2016 AEIT International Annual Conference (AEIT)*, Oct 2016, pp. 1–6.

[16] H. Choi, "Design consideration for interleaved boundary conduction mode pfc using fan9611/12 [application note]," ON Semiconductor, 2009, available https://www.fairchildsemi.com/application-notes/AN/AN-6086.pdf.

[17] C. Buob, "Functionality of line filters - leakage currents in the right perspective [white paper]," Farnell - Element 14, 2007, available http://www.farnell.com/datasheets/1712865.pdf.

[18] "CREE Product Datasheet," CREE, available at http://www.wolfspeed.com/media/downloads/145/C3M0065090J.pdf.

[19] S. Zhao, K. Cao, S. Firwana, A. Swaris, R. Content, and O. Trescases, "Failsafe smart led module with thermal management, string current balancing and commutation for lifetime extension," in *2012 IEEE Energy Conversion Congress and Exposition (ECCE)*, Sept 2012, pp. 4246–4253.